

Monoenergetic High-energy Ion Source via Femtosecond Laser Incident Parallel to a Microplate

X. F. Shen,¹ A. Pukhov,^{1,*} and B. Qiao²

¹*Institut für Theoretische Physik I, Heinrich-Heine-Universität Düsseldorf, 40225 Düsseldorf, Germany*

²*Center for Applied Physics and Technology, HEDPS, SKLNP,
and School of Physics, Peking University, Beijing, 100871, China*

(Dated: November 27, 2024)

Using fully three-dimensional particle-in-cell simulations, we show that readily available femtosecond laser systems can stably generate proton beams with hundred MeV energy and low spread at $\sim 1\%$ level by parallel irradiation of a tens of micrometers long plasma plate. As the laser pulse sweeps along the plate, it drags out a huge charge (~ 100 nC) of collimated energetic electrons and accelerates them along the plate surface to superponderomotive energies. When this dense electron current arrives at the rear end of the plate, it induces a strong electrostatic field. Due to the excessive space charge of electrons, the longitudinal field becomes bunching while the transverse field is focusing. Together, this leads to a highly monoenergetic energy spectrum and much higher proton energy as compared to simulation results from typical target normal sheath acceleration and radiation pressure acceleration at the same laser parameters.

PACS numbers: 52.38.Kd, 41.75.Jv, 52.38.-r, 52.27.Ny

The research of laser-driven ion acceleration received renewed interest in recent years due to several breakthroughs achieved in experiments [1–4] and the forthcoming petawatt laser devices [5]. The maximum proton energy has been improved from 58MeV [6] to 94MeV [4] with advancements in both laser technology and targetry. However, the ion beams still exhibit an exponentially decaying energy distribution. This is a major drawback to cancer therapy and other applications, which require energy spread only about 1% [7–9]. An energy-selection system out of a broad energy spectrum ion source sophisticates the device and leads to huge particle loss [10, 11]. Meanwhile, most of experiments are accomplished on large laser facilities which deliver 100s J energy within a picosecond at low repetition rate [1, 2, 4, 6]. These lasers can be operated only in a few national laboratories [5]. Compared to this, a high-repetition-rate, low-cost and stable femtosecond laser is more preferable for developing the future compact ion sources. Actually, 100 Terawatt (TW)-class femtosecond laser systems have been distributed widely around the world and also many multi-petawatt (PW) ones are currently operational, under construction or in the planning phase [5], for which generation of monoenergetic high-energy ion beams is one of primary applications. Nevertheless, in the present femtosecond laser-ion acceleration experiments, proton energies are typically much lower than those obtained from picosecond laser pulses and the energy spectra are also broad [12–17].

To achieve monoenergetic ion beams, a longitudinal bunching accelerating field is important, in which fast ions experience a smaller field and the slow ones a larger field. In traditional radio-frequency accelerators, such a bunching field is realized through controlling the phase of the synchronous particle relative to the crest of the

accelerating wave [18], while in laser-ion acceleration, it appears as a longitudinal negative gradient electric field acting on the accelerated ions. In one of the mostly investigated laser-ion acceleration mechanisms, radiation pressure acceleration (RPA) [19–22], such a bunching field was supposed to exist through piling excessive electrons at the rear surface. However, to obtain monoenergetic ion beams, the RPA requires ultraintense laser pulses ($> 10^{22}$ W/cm²) and a large spot size simultaneously, which remains a big challenge in experiments even for multi-PW lasers. In addition, the RPA is plagued by strong electron heating due to effects of transverse instabilities [23] and finite spot size [13]. These may induce relativistic transparency and destroy the bunching electric field. As a consequence, the obtained ion energy is rather limited and energy spread is very large.

In the other widely studied mechanism, target normal sheath acceleration (TNSA) [24–27], this longitudinal bunching field is absent due to the low density of energetic electrons. The energy spectrum of TNSA ions is characterized by an exponential decay. Moreover, the acceleration time is related to laser pulse duration, which undoubtedly leads to much lower energy with femtosecond laser pulses [28, 29].

Many efforts have been devoted to overcoming the limitations of these mechanisms to improve the ion beam parameters, especially the maximum energy and energy spread. Here, we may mention target designs [16, 26, 30, 31], multi-pulse schemes [32, 33], post-acceleration [34] and novel mechanisms [35–40]. Nevertheless, the obtained energy spreads are still larger than 10% due to the absence of a self-established bunching field, and also the increasing complexity in the laser pulse and target configurations may reduce the repetition-rate and robustness of experiments. Therefore, the future of

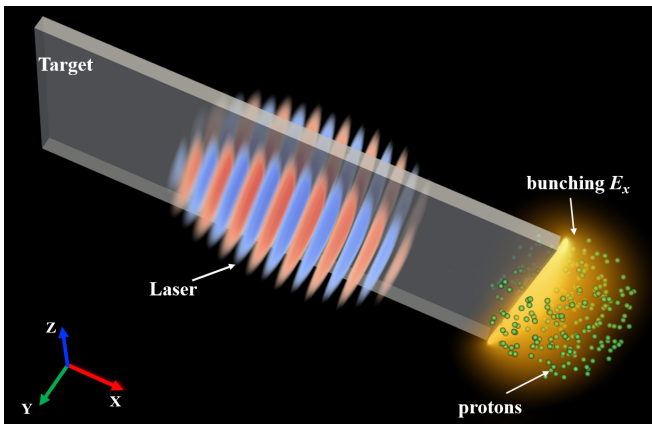


FIG. 1. (color online) Schematic of ion acceleration mechanism via a femtosecond laser (red-blue) incident parallel to a micro-scale plate (grey). The yellow domain shows the distribution of the longitudinal bunching field and green dots represent accelerated ions. Here the schematic does not represent the true scale, where an infinitely long plate along z direction can be used in experiment.

producing high-energy (like 100MeV protons), monoenergetic (energy spread about 1%) ion beams with the known mechanisms is vague.

In this Letter, we show that a longitudinal bunching accelerating field is built spontaneously when a currently available femtosecond laser pulse is incident on an edge of a simple micro-scale plasma plate, parallel to its surface, as shown by Fig. 1. As the laser pulse of intensity $> 10^{20}$ W/cm² sweeps along the plate, it extracts abundant buckets of electrons from the plate into vacuum and accelerates them forward along the plate surface to superponderomotive energies via direct laser acceleration (DLA) [41] and surface plasma wave (SPW) [42, 43]. The charge of energetic electrons (many tens to hundreds of nC) injected into the accelerating region at the rear edge of the plate is much larger than that of protons placed there (just a few nC). This ensures that the protons near the laser propagation axis are surrounded by the excessive space charge of electrons, that leads to a negative gradient longitudinal bunching field and also a transverse focusing field. Finally, a quasi-monoenergetic proton beam with peak energy > 100 MeV, energy spread about 1% and particle number $\sim 10^9$ can be stably obtained.

The three-dimensional (3D) particle-in-cell (PIC) simulations are conducted with the EPOCH code [44] and the VLPL code [45]. The simulation box is $120\lambda \times 40\lambda \times 52.5\lambda$ in the $x \times y \times z$ directions, containing $2400 \times 1600 \times 1050$ cells, respectively. Here, a higher resolution in y direction is used to resolve the plasma skin depth and the process of electrons extraction out from the plate, since a y -polarized laser pulse is chosen. We use larger box length in z direction because of a large plate to mimic the real experimental situation. The

laser intensity is $I_0 = 7.8 \times 10^{20}$ W/cm² with the wavelength $\lambda = 800$ nm. The laser pulse has the Gaussian profile in both space and time with the radius $r_L = 7.5\lambda$ and pulse duration $\tau_L = 45$ fs, respectively, which is focused at the front edge of the plate. A plasma plate of high-Z material (we assumed gold) had the dimensions $x \times y \times z = 43.75\lambda \times 0.75\lambda \times 45\lambda$. Its rear end has been covered by a hydrocarbon (CH) layer. To reduce the computational resources, the electron densities for the plasma plate and CH layer are both chosen as relativistically overdense $n_e = 30n_c$. Here $n_c = \pi m_e c^2 / e^2 \lambda^2$ is the critical density. The initial charge states of ions are given according to the Ammosov-Delone-Krainov formula [46], which means the ion species are Au⁵¹⁺ in the main target, C⁶⁺ and H⁺ in the hydrocarbon layer. The transverse dimensions of the CH layer are $0.75\lambda \times 45\lambda$ (same as the plate), while the longitudinal is set to $l_x = 0.4\lambda$ to ensure the proton charge realistic. The density ratio of proton to carbon ion is $n_p : n_{C^{6+}} = 1 : 1$. The macroparticles in each cell for electrons, gold ions, carbon ions and protons are 8, 1, 8 and 32, respectively. Open boundary conditions for fields and particles are employed. The numerical convergence has been confirmed via compar-

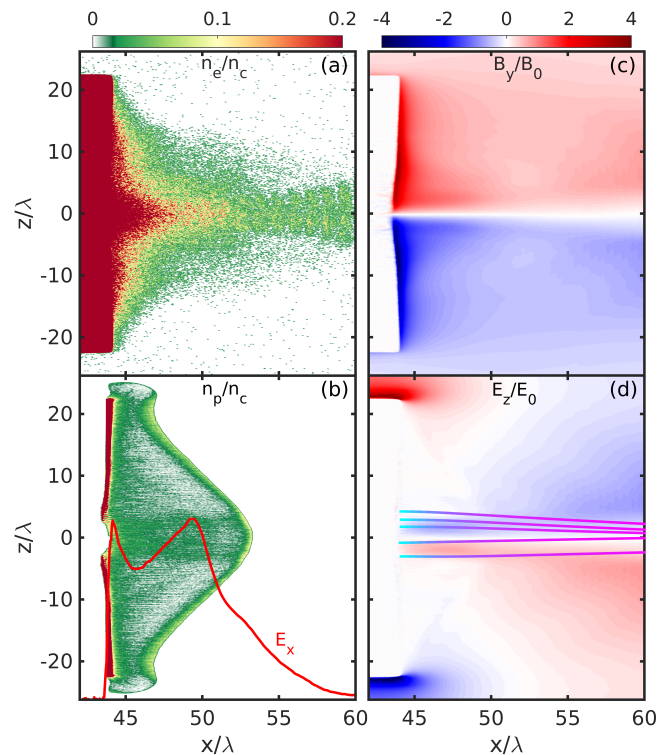


FIG. 2. (color online) (a) and (b) show the distributions of electron and proton density in (x, z) plane at $t = 82T_0$, respectively. The red line in (b) displays the on-axis profile of the accelerating field E_x . (c) and (d) show the transverse magnetic field B_y and electric field E_z , respectively. The lines in (d) correspond to the collimated trajectories of selected protons, where the color represents the proton energy.

ing the interested physical quantities with simulations at different resolutions and the two codes.

Figure 2(a) shows the electron density distribution in (x, z) plane at $t=82T_0$, where $t = 0$ represents the time when the pulse peak enters the simulation box. One sees that the electron beam exiting the plate is highly collimated. This is because, as the laser pulse sweeps along the plasma plate, electrons within the skin depth are continuously ripped off by the laser electric field E_y and accelerated forward via the mixed DLA and SPW mechanisms. Both of them contribute to the increments of p_x , resulting in $p_x \gg p_\perp \gg m_e c$ [41, 42, 47]. For DLA, it is due to the $\mathbf{v} \times \mathbf{B}$ force and for SPW, it is the longitudinal surface plasmon field [48]. The SPW can be easily excited when a laser pulse is incident along an overdense plasma surface with a sharp edge, and then travels along the plate with velocity close to c [42, 43]. Such an acceleration benefits from a long plate irradiated by the center of laser pulse. It promises longer acceleration distance and larger electron charge compared to a grating target, and it does not require specific modulations [49, 50]. After electrons are injected into the vacuum, a transverse focusing magnetic field B_y is induced, as shown by Fig. 2(c), which offsets the defocusing force of Coulomb field E_z [shown by Fig. 2(d)].

The space charge of this collimated electron beam is huge. When the laser pulse reaches the rear surface, the charge of high energy electrons ($\gamma_e > 10$) outside of the plate is about 150nC ($\sim 10^{12}$), which accords well with the estimation of $N_e = 4r_L l_s l_p n_e$, where l_p is the plate length, $l_s = c/\omega_{pe}$ is the skin depth and $\omega_{pe} = \sqrt{4\pi n_e e^2/m_e}$ is the plasma frequency. Then, a large part of them are continuously injected into the ion acceleration region, where the electron space charge can reach about 50nC , much larger than the charge of protons (about 2.7nC within the focus spot). This ensures that protons, especially those around the propagation axis, are surrounded by a negative electron cloud during the acceleration process. The distribution of proton density in (x, z) plane is shown in Fig. 2(b), which is much lower than the electron density [Fig. 2(a)], even at the compressed density peak. In one dimensional situation, $\partial E_x/\partial x = -4\pi e(n_e - n_p)$. Therefore, a longitudinal bunching electric field forms around protons, as the red line shown in Fig. 2(b), like the ‘‘compressed electron layer’’ in RPA [51, 52], which compresses the proton phase space [Fig. 3(a)] and reduces the energy spread [solid lines in Fig. 4(b)] repeatedly. This is the reason for the formation of a proton density peak in Fig. 2(b).

Meanwhile, for protons, the E_z field provides a focusing force, while B_y is defocusing. However, since E_z is comparable to B_y and the velocities of protons v_x are smaller than the light speed, protons are actually focused by these transverse fields. We show trajectories of some selected protons in Fig. 2(d), where the color marks the evolution of proton energy. Moreover, we can

also see more protons gather around the x -axis in Fig. 2(b). Such a self-established longitudinal bunching and transverse focusing field configuration makes our scheme robust and suitable for generation of monoenergetic ion beams. This is the key difference from the typical TNSA, where a debunching field dominates the acceleration process. Furthermore, compared to the requirement of a fragile balance condition in RPA [22, 23], the bunching field in our scheme is self-established on the basis of large number of high-energy electrons, which is very robust only if the plate is long enough to provide sufficient charge of electrons.

Figure 3(b) shows the 3D perspective view of proton distribution at the end of acceleration, where the color marks the proton energy and the local density of dots indicates that of proton, since each dot was randomly selected and has the same weight. We see that the highest energy protons gather around the propagation axis (red region), forming a high-density ($\sim 0.1n_c$), high-energy ($> 100\text{MeV}$) quasi-monoenergetic proton bunch.

Further, the red line in Fig. 4(a) represents the electron effective temperature T_{eff} at $t = 50T_0$, which is about 36MeV , much larger than the value of 6.4MeV

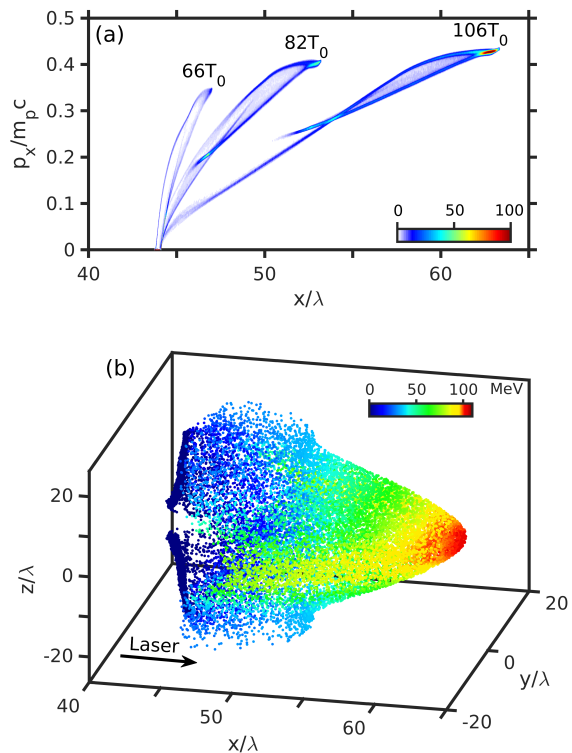


FIG. 3. (color online) (a) Evolution of proton phase space, where the protons are selected within a 10° divergence angle and the color represents the relative proton number. (b) 3D image of the proton distribution at $t = 106T_0$, where the color shows the energy and the local density of dots indicates that of proton. Each dot represents 200 macro-particles.

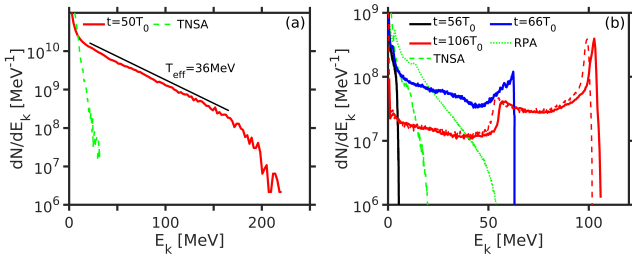


FIG. 4. (color online) Energy spectra of electrons (a) and protons (b). In (b), the black, blue and red solid lines show the evolution of proton energy spectra in our scheme at $t = 56T_0$, $66T_0$ and $106T_0$, respectively. The red dashed line displays the results with a misalignment of 2λ along y direction. Moreover, the green dashed lines in (a) and (b) represents the corresponding energy spectra obtained from typical TNSA, while the green dotted line in (b) shows the results from RPA, where the electron and proton number multiply a factor of 0.1 and 0.01, respectively, to make it suitable to the coordinate range. Note that here protons are selected inside a 10° divergence angle.

given by ponderomotive scaling $T_{\text{pond}} = (\sqrt{1 + a_0^2/2} - 1)m_e c^2$ [41, 53]. The electron density is also high, about $n_h = 2.5n_c$, when electrons are attracted to flow into the mid-plane from both sides. The initial longitudinal field $E_{sh} = \sqrt{8\pi n_h T_{\text{eff}}/e_N} = 4.54 \times 10^{13}$ V/m with $e_N \approx 2.71828$ [28], is consistent with the simulation result 5.0×10^{13} V/m, which is almost comparable to the peak value of laser field. Due to the collimation and large longitudinal recirculation radii of high-energy electron beams, E_x decays only slowly and the acceleration of the high-energy protons could last for 150fs (about four times longer than τ_L). This strong, long-lasting accelerating field leads to a high efficient acceleration, which also explains why almost all the protons near x -axis are evacuated in Fig. 2(b).

Figure 4(b) shows the energy spectra of proton beam at different times. At the beginning, the energy spread is large (black line), since protons feel a positive gradient E_x as they are pulled out from the CH layer. Subsequently, the energy spread decreases constantly due to the longitudinal bunching field caused by excessive electrons, as shown by the blue and red lines. Finally, a high-energy quasi-monoenergetic proton beam, with peak energy >100 MeV, energy spread about 1.17% and particle number 8×10^8 (0.13nC) within the peak (FWHM), is obtained (red line). This low energy spread persists for a long time since the further contribution of Coulomb explosion could be ignored considering the co-propagating, collimated electron beam. Note that our results is very robust, which is not sensitive to a possibly slight misalignment [red dashed line in 4(b)], variation of target dimensions (length, thickness or height) [54], and existence of preplasma [54].

Moreover, as a baseline comparison, we also performed

3D simulations with a laser pulse obliquely incident on a flat target with incidence angle 30° , where the laser parameters keep the same. The electron and proton energy spectra are shown by the dashed green lines in Fig. 4(a) and 4(b), respectively. The effective temperature is much lower and the maximum proton energy is about five times less than that in our scheme and the energy spectrum is broad. Furthermore, the green dashed-dotted line shows the results from a target with area density satisfying the optimal condition of RPA [52]. Due to the effects of instabilities [23], the energy spectrum is exponentially decaying and the maximum energy is only half of ours.

Figure 5 illustrates the peak proton energy ϵ_p (black asterisks) and energy spread (red triangles) as a function of laser intensity I_0 obtained from 3D simulations, where the other parameters keep almost the same. The numerical results suggest that the scaling of ϵ_p satisfies $\epsilon_p \sim \alpha(I_0/I_{18})^{1/2}$, with coefficient $\alpha \approx 3.5$ MeV and $I_{18} = 10^{18}$ W/cm 2 . Though the scaling is similar to that of TNSA, the proportionality factor α is significantly higher, as we discussed before. This stems from the high-quality electron beam characterized with large particle number, high effective temperature and small divergence angle. More importantly, as the red triangles shown in Fig. 5, the energy spread always stays at an extremely low level, and even with moderate intensity $I_0 < 10^{20}$ W/cm 2 , it is still less than 10%. Proton beams with an energy spread at 1% level can be stably obtained as the laser intensity increases. To the best of our knowledge, no experiments or 3D PIC simulations of laser-ion acceleration have reported such high-quality ion beams [8, 9, 55]. Though in Ref. [56], proton beams with energy spread 1% were achieved, but only $\sim 10^5$ protons within peak and the experiments are performed with CO $_2$ laser

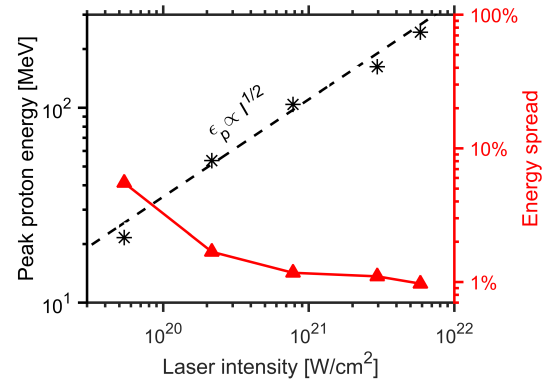


FIG. 5. (color online) The peak proton energy ϵ_p (black asterisks) and energy spread (red triangles) with varying laser intensity, where the other parameters are kept almost the same as those of Fig. 2, except the electron density to avoid the relativistic transparency. The dashed black line displays the best fit scaling for peak proton energy.

systems.

In conclusion, a robust scheme for achieving 100MeV proton beams with energy spread at the $\sim 1\%$ level is proposed, where a longitudinal bunching and transverse focusing field is self-established through irradiating a femtosecond laser pulse parallel to a micro-scale plate. This novel interaction geometry not only promises a high-quality proton beam, but also enables other fundamental studies and various applications. For example, as the high-energy electrons move forward, a large return current and therefore a strong quasistatic magnetic field is induced, which could compress the plasma to an ultra-high density [54, 57]. Therefore, a microscale ultradense Z-pinch can be expected to form.

ACKNOWLEDGEMENTS

This work is supported by the DFG (project PU 213/9) and GCS Jülich (project QED20). X.F.S. gratefully acknowledges support by the Alexander von Humboldt Foundation. X.F.S. acknowledges helpful discussions with Ke Jiang at HHU.

* Correspondence should be addressed to: pukhov@tp1.uni-duesseldorf.de

- [1] S. A. Gaillard, T. Kluge, K. A. Flippo, M. Bussmann, B. Gall, T. Lockard, M. Geissel, D. T. Offermann, M. Schollmeier, Y. Sentoku, *et al.*, *Phys. Plasmas* **18**, 056710 (2011).
- [2] F. Wagner, O. Deppert, C. Brabetz, P. Fiala, A. Kleinschmidt, P. Poth, V. A. Schanz, A. Tebartz, B. Zielbauer, M. Roth, *et al.*, *Phys. Rev. Lett.* **116**, 205002 (2016).
- [3] I. J. Kim, K. H. Pae, I. W. Choi, C.-L. Lee, H. T. Kim, H. Singhal, J. H. Sung, S. K. Lee, H. W. Lee, P. V. Nickles, *et al.*, *Phys. Plasmas* **23**, 070701 (2016).
- [4] A. Higginson, R.J. Gray, M. King, R.J. Dance, S.D.R. Williamson, N.M.H. Butler, R. Wilson, R. Capdessus, C. Armstrong, J.S. Green, *et al.*, *Nat. Commun.* **9**, 724 (2018).
- [5] C. Danson, D. Hillier, N. Hopps, and D. Neely, *High Power Laser Sci. Eng.* **3**, e3 (2015).
- [6] R. A. Snavely, M. H. Key, S. P. Hatchett, T. E. Cowan, M. Roth, T. W. Phillips, M. A. Stoyer, E. A. Henry, T. C. Sangster, M. S. Singh, *et al.*, *Phys. Rev. Lett.* **85**, 2945 (2000).
- [7] S. V. Bulanov, T. Z. Esirkepov, V. S. Khoroshkov, A. V. Kuznetsov, and F. Pegoraro, *Phys. Lett. A* **299**, 240 (2002).
- [8] A. Macchi, M. Borghesi, and M. Passoni, *Rev. Mod. Phys.* **85**, 751 (2013).
- [9] H. Daido, M. Nishiuchi and A. S. Pirozhkov, *Rep. Prog. Phys.* **75**, 056401 (2012).
- [10] U. Linz and J. Alonso, *Phys. Rev. Accel. Beams*, **19**, 124802 (2016).
- [11] U. Masood, M. Bussmann, T. E. Cowan, W. Enghardt, L. Karsch, F. Kroll, U. Schramm, J. Pawelke, *Appl. Phys. B* **117**, 41 (2014).
- [12] A. Henig, S. Steinke, M. Schnürer, T. Sokollik, R. Hörlein, D. Kiefer, D. Jung, J. Schreiber, B. M. Hegelich, X. Q. Yan, J. Meyer-ter-Vehn, *et al.*, *Phys. Rev. Lett.* **103**, 245003 (2009).
- [13] F. Dollar, C. Zolick, A. G. R. Thomas, V. Chvykov, J. Davis, G. Kalinchenko, T. Matsuoka, C. McGuffey, G. M. Petrov, L. Willingale, *et al.*, *Phys. Rev. Lett.* **108**, 175005 (2012).
- [14] C. Scullion, D. Doria, L. Romagnani, A. Sgattoni, K. Naughton, D. R. Symes, P. McKenna, A. Macchi, M. Zepf, S. Kar, *et al.*, *Phys. Rev. Lett.* **119**, 054801 (2017).
- [15] U. Schramm, M. Bussmann, A. Irman, M. Siebold, K. Zeil, D. Albach, C. Bernert, S. Bock, F. Brack, J. Branco, *et al.*, *IOP Conf. Series: Journal of Physics: Conf. Series* **874**, 012028 (2017).
- [16] J. H. Bin, M. Yeung, Z. Gong, H. Y. Wang, C. Kreuzer, M. L. Zhou, M. J. V. Streeter, P. S. Foster, S. Cousens, B. Dromey, *et al.*, *Phys. Rev. Lett.* **120**, 074801 (2018).
- [17] N. P. Dover, M. Nishiuchi, H. Sakaki, Ko. Kondo, M. A. Alkhimova, A. Ya. Faenov, M. Hata, N. Iwata, H. Kiriya, J. K. Koga, *et al.*, *Phys. Rev. Lett.* **124**, 084802 (2020).
- [18] T. P. Wangler, *Principles of RF Linear Accelerators* (John Wiley & Sons Inc, New York, 1998), p. 172
- [19] T. Esirkepov, M. Borghesi, S. V. Bulanov, G. Mourou, and T. Tajima, *Phys. Rev. Lett.* **92**, 175003 (2004).
- [20] A. P. L. Robinson, M. Zepf, S. Kar, R. G. Evans, and C. Bellei, *New J. Phys.* **10**, 013021 (2008).
- [21] B. Qiao, M. Zepf, M. Borghesi, and M. Geissler, *Phys. Rev. Lett.* **102**, 145002 (2009).
- [22] X. F. Shen, B. Qiao, H. Zhang, S. Kar, C. T. Zhou, H. X. Chang, M. Borghesi, and X. T. He, *Phys. Rev. Lett.* **118**, 204802 (2017).
- [23] F. Pegoraro and S. V. Bulanov, *Phys. Rev. Lett.* **99**, 065002 (2007); Y. Wan, I. A. Andriyash, W. Lu, W. B. Mori, and V. Malka, *Phys. Rev. Lett.* **125**, 104801 (2020).
- [24] A. Pukhov, *Phys. Rev. Lett.* **86**, 3562 (2001).
- [25] S. C. Wilks, A. B. Langdon, T. E. Cowan, M. Roth, M. Singh, S. Hatchett, M. H. Key, D. Pennington, A. MacKinnon, and R. A. Snavely, *Phys. Plasmas* **8**, 542 (2001).
- [26] H. Schwoerer, S. Pfoth, O. Jäeckel, K.-U. Amthor, B. Liesfeld, W. Ziegler, R. Sauerbrey, K. W. D. Ledingham, and T. Esirkepov, *Nature (London)* **439**, 445 (2006).
- [27] M. Nakatsutsumi, Y. Sentoku, A. Korzhimanov, S.N. Chen, S. Buffechoux, A. Kon, B. Atherton, P. Audebert, M. Geissel, L. Hurd, *et al.*, *Nat. Commun.* **9**, 280 (2018).
- [28] P. Mora, *Phys. Rev. Lett.* **90**, 185002 (2003).
- [29] J. Fuchs, P. Antici, E. d’Humières, E. Lefebvre, M. Borghesi, E. Brambrink, C. A. Cecchetti, M. Kaluza, V. Malka, M. Manclossi, *et al.*, *Nat. Phys.* **2**, 48 (2006).
- [30] M. Chen, A. Pukhov, T. P. Yu, Z.-M. Sheng, *Phys. Rev. Lett.* **103**, 024801 (2009).
- [31] T. Bartal, M. E. Foord, C. Bellei, M. H. Key, K. A. Flippo, S. A. Gaillard, D. T. Offermann, P. K. Patel, L. C. Jarrott, D. P. Higginson, *et al.*, *Nat. Phys.* **8**, 139 (2012).
- [32] T. Toncian, M. Borghesi, J. Fuchs, E. d’Humières, P. Antici, P. Audebert, E. Brambrink, C. A. Cecchetti, A. Pipahl, L. Romagnani, and O. Willi, *Science* **312**, 410

- (2006).
- [33] K. Markey, P. McKenna, C. M. Brenner, D. C. Carroll, M. M. Günther, K. Harres, S. Kar, K. Lancaster, F. Nürnberg, M. N. Quinn, *et al.*, Phys. Rev. Lett. **105**, 195008 (2010).
- [34] S. Kar, H. Ahmed, R. Prasad, M. Cerchez, S. Brauckmann, B. Aurand, G. Cantonono, P. Hadjisolomou, C. L. S. Lewis, A. Macchi, *et al.*, Nat. Commun. **7**, 10792 (2016).
- [35] P. Hilz, T.M. Ostermayr, A. Huebl, V. Bagnoud, B. Borm, M. Bussmann, M. Gallei, J. Gebhard, D. Haffa, J. Hartmann, *et al.*, Nat. Commun. **9**, 423 (2018).
- [36] A. V. Brantov, E. A. Govras, V. F. Kovalev, and V. Yu. Bychenkov, Phys. Rev. Lett. **116**, 085004 (2016).
- [37] F. Mackenroth, A. Gonoskov, and M. Marklund, Phys. Rev. Lett. **117**, 104801 (2016).
- [38] R. Matsui, Y. Fukuda, and Y. Kishimoto, Phys. Rev. Lett. **122**, 014804 (2019).
- [39] X. F. Shen, B. Qiao, H. Zhang, Y. Xie, S. Kar, M. Borghesi, M. Zepf, C. T. Zhou, S. P. Zhu, and X. T. He, Appl. Phys. Lett. **114**, 144102 (2019).
- [40] T. Ziegler, C. Bernert, S. Bock, F.-E. Brack, T. E. Cowan, N.P. Dover, M. Garten, L. Gaus, R. Gebhardt, U. Helbig, *et al.*, arXiv e-prints arXiv:2007.11499, (2020)
- [41] A. Pukhov, Z. -M. Sheng, and J. Meyer-ter-Vehn, Phys. Plasmas, **6**, 2847 (1999).
- [42] C. Riconda, M. Raynaud, T. Vialis, and M. Grech, Phys. Plasma, **22**, 073103 (2015); A. Macchi, Phys. Plasma, **25**, 031906 (2018).
- [43] J. M. Pitarke, V. M. Silkin, E. V. Chulkov and P. M. Echenique, Rep. Prog. Phys. **70**, 1 (2007).
- [44] T. D. Arber, K. Bennett, C. S. Brady, A. Lawrence-Douglas, M. G. Ramsay, N. J. Sircombe, P. Gillies, R. G. Evans, H. Schmitz, A. R. Bell and C. P. Ridgers, Plasma Phys. Control. Fusion **57**, 113001 (2015).
- [45] A. Pukhov, “Particle-In-Cell Codes for Plasma-based Particle Acceleration”, CERN Yellow Rep. 1 , 181 (2016).
- [46] M. V. Ammosov, N. B. Delone and V. P. Krainov, Sov. Phys. JETP, **64**, 1191 (1986).
- [47] A. Pukhov and J. Meyer-ter-Vehn Appl. Phys. B **74**, 355 (2002).
- [48] T. Kluge, S. A. Gaillard, K. A. Flippo, T. Burris-Mog, W. Enghardt, B. Gall, M. Geissel, A. Helm, S. D. Kraft, T. Lockard, *et al.*, New J. Phys. **14**, 023038 (2012).
- [49] L. Fedeli, A. Sgattoni, G. Cantonono, D. Garzella, F. Réau, I. Prencipe, M. Passoni, M. Raynaud, M. Květoň, J. Proška, *et al.*, Phys. Rev. Lett. **116**, 015001 (2016).
- [50] L. Chopineau, A. Leblanc, G. Blaclard, A. Denoeud, M. Thévenet, J-L. Vay, G. Bonnaud, Ph. Martin, H. Vincenti, and F. Quéré, Phys. Rev. X **9**, 011050 (2019).
- [51] X. Q. Yan, C. Lin, Z.-M. Sheng, Z. Y. Guo, B. C. Liu, Y. R. Lu, J. X. Fang, and J. E. Chen, Phys. Rev. Lett. **100**, 135003 (2008).
- [52] A. Macchi, S. Veghini, and F. Pegoraro, Phys. Rev. Lett. **103**, 085003 (2009).
- [53] S. C. Wilks, W. L. Kruer, M. Tabak, and A. B. Langdon, Phys. Rev. Lett. **69**, 1383 (1992).
- [54] See Supplemental Material for details. It mainly includes the discussions about the robustness of scheme to the variation of plate dimensions (length, thickness and height) and the existence of preplasmas.
- [55] B. Qiao, X. F. Shen, H. He, Y. Xie, H. Zhang, C. T. Zhou, S. P. Zhu, and X. T. He, Plasma Phys. Control. Fusion **61**, 014039 (2019).
- [56] D. Haberberger, S. Tochitsky, F. Fiuza, C. Gong, R. A. Fonseca, L. O. Silva, W. B. Mori and C. Joshi, Nat. Phys. **8**, 95 (2012).
- [57] V. Kaymak, A. Pukhov, V. N. Shlyaptsev and J. J. Rocca, Phys. Rev. Lett. **117**, 035004 (2016).